

Available online at www.sciencedirect.com

jmr&t
Journal of Materials Research and Technology
journal homepage: www.elsevier.com/locate/jmrt



Original Article

Comparison of morphology and compressive deformation behavior of copper foams manufactured via freeze-casting and space-holder methods



Kicheol Hong^a, Csilla Kádár^{b,c,d}, Michal Knapek^e, Daria Drozdenko^{e,f}, Péter Jenei^b, Myung-Yeon Kim^a, Heeman Choe^a, Kristián Máthis^{e,***}, Hyeji Park^{a,**}, Jenő Gubicza^{b,*}

^a School of Materials Science & Engineering, Kookmin University, 77 Jeongneung-ro, Seongbuk-gu, Seoul, 02707, Republic of Korea

^b Department of Materials Physics, Eötvös Loránd University, Budapest, P.O.B. 32, H-1518, Hungary

^c Department of Materials Science and Engineering, Budapest University of Technology and Economics, Műegyetem Rakpart 3., H-1111 Budapest, Hungary

^d MTA–BME Lendület Composite Metal Foams Research Group, Műegyetem Rakpart 3., H-1111, Budapest, Hungary

^e Department of Physics of Materials, Charles University, Ke Karlovu 5, CZ12116 Prague 2, Czech Republic

^f Nuclear Physics Institute of the Czech Academy of Sciences, Hlavní 130, 250 68 Řež-Husinec, Czech Republic

ARTICLE INFO

Article history:

Received 29 September 2021

Accepted 22 November 2021

Available online 27 November 2021

Keywords:

Copper

Foam

Freeze-casting

Space-holder

Deformation

Acoustic emission

ABSTRACT

Copper (Cu) foams with high porosity of about 63–78% were processed by the freeze-casting (FC) and space-holder (SH) methods. The FC and SH techniques yielded lamellar and polygonal pore structures, respectively, with similar porosities. The deformation behaviors of the two different types of Cu foams were compared using uniaxial compression and a simultaneous acoustic emission (AE) and video recording analysis. It was found that the compressive yield strength values for the FC-Cu and SH-Cu foams were significantly different, which were 19–29 MPa and 1.2–2.3 MPa, respectively. Furthermore, the energy absorbed during compression up to the strain of 50% was obtained as $\sim 12.3 \text{ MJ m}^{-3}$ and $\sim 2.7 \text{ MJ m}^{-3}$ for the FC-Cu and SH-Cu foams, respectively, resulting in approximately 4.6 times higher energy absorption capability for the FC-Cu foam. The deformation processes occurring during compression in the two Cu foams were studied by the AE and image analysis. The video and the evaluated AE parameters (e.g., the AE voltage, the cumulative number of events, and the cumulative energy) revealed that, in the case of the FC foam, the localized fracture of the struts within a well-defined single deformation band took place, which gave rise to pronounced AE signals (mostly in the plateau stage of compression). By contrast, the deformation was highly

* Corresponding author.

** Corresponding author.

*** Corresponding author.

E-mail addresses: mathis@met.mff.cuni.cz (K. Máthis), hyeji@kookmin.ac.kr (H. Park), jeno.gubicza@ttk.elte.hu (J. Gubicza).<https://doi.org/10.1016/j.jmrt.2021.11.108>2238-7854/© 2021 The Author(s). Published by Elsevier B.V. This is an open access article under the CC BY license (<http://creativecommons.org/licenses/by/4.0/>).

homogeneous in the case of the SH-Cu foam, and the main deformation mechanisms were gradual bending and buckling of the foam struts during compression.

© 2021 The Author(s). Published by Elsevier B.V. This is an open access article under the CC BY license (<http://creativecommons.org/licenses/by/4.0/>).

1. Introduction

Copper (Cu) has been utilized for a wide range of industrial applications owing to its excellent electrical/thermal conductivity, appropriate reduction potential, and antimicrobial action [1–6]. For a variety of functional applications, porous Cu materials, also generally called Cu foams, have recently been considered potential candidates for use in lithium-ion batteries [7], supercapacitors [8], catalysts [9], heat sinks [10], and filters [11] because of their unique advantages such as large specific surface area (for efficient electrochemical reaction) and high liquid/gas permeability (for rapid mass and heat transfer).

For the applications described above, the optimal pore size differs. For example, the required Cu foam's pore size ranges from 5 ppi to 60 ppi (pores per inch) for heat exchanger applications, e.g., in refrigeration and air conditioning systems [12–17] and the foam filters for cleaning secondary-treated wastewater contaminated with bacteria demand smaller pores, i.e., 110 ppi or so [11]. In the cases of catalysts, supercapacitors, and batteries, the specific surface area is the determining factor, which can be generally increased by decreasing the pore size at a given foam density [18,19].

Numerous studies have already been reported on the microstructural and mechanical properties of Cu foams fabricated by various processes, such as vacuum foaming [20], solid–gas eutectic solidification [21], freeze casting (FC) followed by sintering [22], dealloying [23], space holder (SH) [24], and electrodeposition on fugitive templates [25]. Among these, FC and SH are particularly promising as they are scalable, facile, and low-cost methods for manufacturing Cu foams. These methods further enable the control of processing parameters and thus the adjustment of the pore shape, size, and fraction (i.e., porosity). In the case of Cu foams fabricated by the FC method, the porosity and the equivalent ppi (the ppi value calculated from the sizes of the pores and the walls given in the literature) can be adjusted between 45–73% and 200–800 ppi, respectively [22], whereas in the case of Cu foams produced by the SH method, the porosity in the range of 50–85% corresponds to the equivalent ppi values between 2 and 500 according to the reports in [24,26].

The FC method, based on the solidification of a solvent, can produce metallic foams with aligned, elongated open-pore structures replicating the solvent crystal if the selection of powder size, the freezing temperature, and the difference between the ambient and the mold temperatures are well controlled. It involves the following steps: (i) preparation of powder slurry by mixing starting powder and binder in a solvent, (ii) directional freezing of slurry, (iii) sublimation of the solvent crystal, and (iv) solid-state sintering (see Fig. 1a) [22]. The SH method is a representative powder meta

llurgy process for manufacturing of metallic foams with interconnected open pores that replicate the size and shape of the SH agent. This process involves the following steps: (i) physical mixing of metallic powder with space-holding particles, (ii) compaction of powder mixture via a pressing process, (iii) solid-state sintering, and finally (iv) removal of the SH agent (see Fig. 1b) [24].

Among the numerous properties of Cu foams, the mechanical behavior is one of the most important factors because it has a significant influence on the actual performance and durability of the as-processed materials [27–30]. Several previous studies have examined the correlation between the morphology and the mechanical properties of Cu foams subjected to compressive deformation. For instance, Park et al. (FC) [22], Parvavian et al. (SH) [24], Hyun et al. (vacuum foaming) [20], and Chen et al. (electrodeposition) [31] manufactured Cu foams and performed compression tests on them using specimens with different morphological characteristics (e.g., porosity and direction of struts). Nonetheless, there have been few attempts to compare the morphology and compressive deformation behavior of Cu foams manufactured via different processes. In this regard, a comparative evaluation of the morphological and mechanical properties of Cu foams manufactured through various methods could be valuable.

In this study, Cu foams were successfully manufactured by the two promising methods of FC and SH with the average pore size being ~800 ppi and ~200 ppi, respectively. The morphological (i.e., porosity and pore/strut/grain size) and compressive results of the FC- and SH-Cu foams were measured and compared with theoretical models in order to understand the correlation between their morphology, microstructure, and compressive behavior. Additionally, an acoustic emission (AE) analysis was performed during the compression tests of the FC-Cu and SH-Cu foams to investigate the deformation mechanisms in the two Cu foams.

2. Experimental procedures

2.1. Manufacturing of Cu foam via freeze casting process

A starting powder slurry was prepared by suspending 8 vol.% CuO powder (particle size of ~40 nm, purity of 99%, U.S. Research Nanomaterials Inc., USA) in 30 ml of deionized water containing 2.5 wt.% polyvinyl alcohol (PVA, Sigma–Aldrich Co., USA) as a binder. The slurry was dispersed using magnetic stirring for 10 min and an additional sonication for 1 h at room temperature (repeated twice for uniform dispersion). The CuO slurry was then poured into a Teflon mold (55 mm inner diameter) placed on the top surface of a Cu rod, where the bottom of the Cu rod was cooled by liquid nitrogen, and

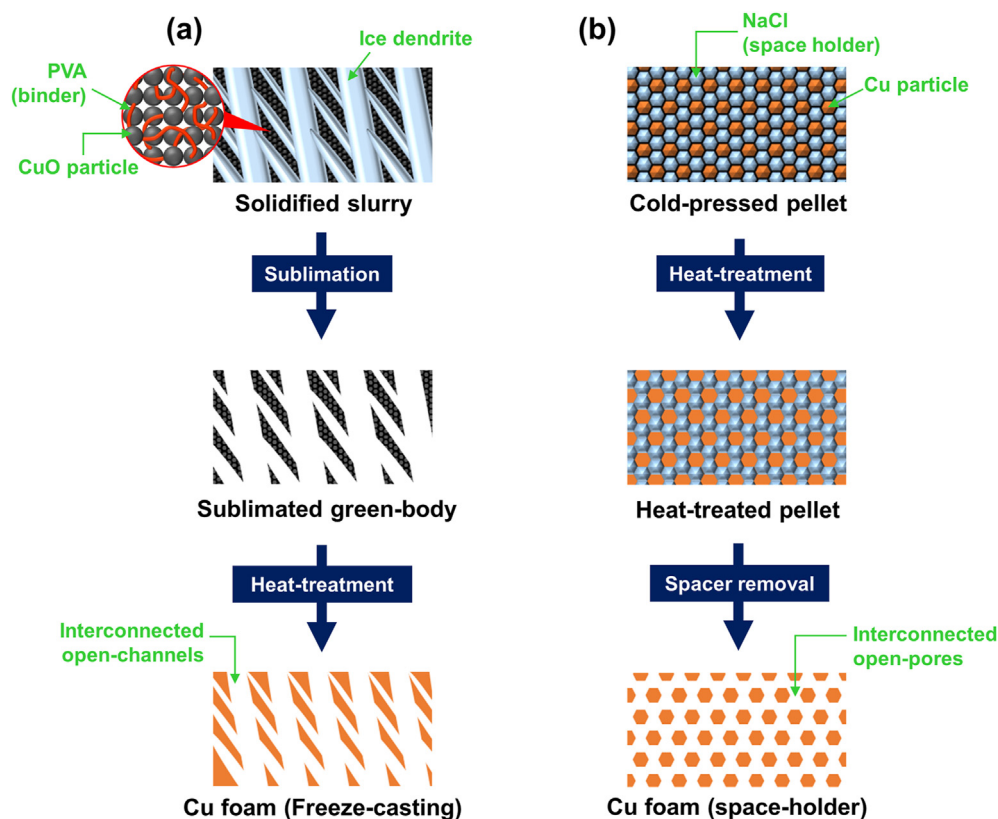


Fig. 1 – Schematic illustration of main steps of Cu foam processing via (a) FC and (b) SH methods.

the temperature of the tip of the Cu rod was controlled at $-10\text{ }^{\circ}\text{C}$ using a heater. The directionally solidified slurry was sublimated for 48 h in a freeze dryer (Operon, FDU-7003, Republic of Korea) at controlled temperature ($-88\text{ }^{\circ}\text{C}$) and pressure (5×10^{-3} torr), resulting in a CuO green body with pore structure replicating the sublimated ice dendrites. The green body was de-binded, reduced from CuO to Cu at $250\text{ }^{\circ}\text{C}$ for 4 h, and then sintered at $800\text{ }^{\circ}\text{C}$ for 10 h under flowing Ar-5% H_2 gas mixture.

2.2. Manufacturing of Cu foam via space holder process

First, NaCl powder (purity of 99%, Alfa Aesar, USA) was milled in a SPEX mill (8000-D Mixer Mill, SPEX SamplePrep, USA) for 30 min with zirconia balls. The ball-milled NaCl and Cu powders (particle size of $\sim 11\text{ }\mu\text{m}$, purity of 99%, Alfa Aesar) were dry-mixed with the volume ratio of 82:18 using the SPEX mill machine. The blended powder mixture was then cold-pressed into pellets at a pressure of 200 MPa for 30 min in a graphite mold (22 mm inner diameter). The Cu green-body pellets were heated in a tube furnace under flowing Ar gas in two steps: the green-body pellets were pre-sintered at $790\text{ }^{\circ}\text{C}$ for 4 h to avoid shape distortion caused by the melting of NaCl at temperatures above $800\text{ }^{\circ}\text{C}$ and then sintered at $830\text{ }^{\circ}\text{C}$ for 4 h to improve their mechanical properties.

2.3. Characterization

The microstructure and composition of the Cu foams were observed using scanning electron microscopy (SEM, JSM7401F,

JEOL, Japan) and X-ray diffraction using a $\text{CuK}\alpha$ radiation source (XRD, Rigaku, D/MAX2500, Japan). The pore size, strut width, and grain size were measured on SEM images using Image-Pro software. In order to observe the grains in the struts of the Cu foams, standard Livingston's etchant (30 ml HCl + 10 ml CH_3COOH + 410 ml H_2O) was applied [32]. The FC- and SH-Cu foams were etched for 30 s and 2 min, respectively. The overall porosity of each foam was acquired by geometrical calculation using the theoretical density of bulk Cu (8.96 g cm^{-3}). In addition, chemical states at the surface of the Cu foams were investigated using X-ray photoelectron spectroscopy using an $\text{AlK}\alpha$ radiation source (XPS, Nexsa, Thermo Fisher Scientific, USA).

Uniaxial compression tests were performed on the FC- and SH-Cu foams using Z020 (Zwick GmbH & Co., Germany) and MTS810 (MTS Systems Corporation, Eden Prairie, USA) mechanical testing machines at ambient temperature. During these experiments, an extensometer was applied at a constant crosshead velocity corresponding to an initial strain rate of 0.001 s^{-1} . The specimens, 8 mm in length and $4 \times 4\text{ mm}^2$ in cross-section, were compressed parallel to their longitudinal axis. In the case of the FC-Cu foam, the loading direction coincided with the direction of freeze casting. The deformation of the specimens was recorded on video and the AE response was detected during compression. The AE signals were measured by a computer-controlled Vallen AMSY-6 system (Vallen Systeme GmbH, Icking, Germany). For both types of Cu foam, the AE signals were detected by a PAC Micro30S broadband sensor and a pre-amplifier providing a gain of 40 dB was used. The AE signals were recorded in the so-

called waveform streaming mode, where no threshold level was set and the AE data were analyzed by post-processing. For the individualization of AE events, a threshold level of 0.03 mV was applied. The hit definition and lockout times were 400 μ s and 800 μ s, respectively. Two main parameters of the AE events were determined: the cumulative number of AE events and the cumulative AE energy.

3. Results and discussion

Figure 2 shows the XRD patterns of the FC- (after reduction and sintering) and SH- (after solid-state sintering) Cu foams compared with the reference peak positions of pure metallic Cu (JCPDS #00-004-0836). The XRD results of the FC- and SH-Cu foams indicate that (i) after reduction/sintering of the FC-CuO green body in the Ar-5% H₂ gas atmosphere, CuO powder was completely transformed into metallic Cu and (ii) the spacer (NaCl) was fully dissolved in warm water (~90 °C) and noticeable formation of byproduct did not occur during the SH procedure.

Figure 3 and Table 1 show the microstructural analysis results of the FC- and SH-Cu foams. The top and side views of a selected FC-Cu foam, showing the surfaces perpendicular and parallel to the freezing direction, are presented in Fig. 3a and c, respectively. Due to the nearly parallel ice growth to the temperature gradient direction of freezing, colonies of aligned, elongated wall-type Cu struts (13 ± 8 μ m in thickness) were formed and surrounded by directional lamellar pores (12 ± 5 μ m in width) replicating the ice dendrite [33]. Single struts of the FC-Cu foam can be seen in the magnified micrographs in Fig. 3a and c, which exhibits one-side-predominant grainy struts formed owing to the competition between the thermal and interfacial energies created during freezing [34–36]. Figs. 3b and d shows the cross and longitudinal sections of the SH-Cu foam, lying perpendicular and parallel to the cold-pressing direction during SH processing,

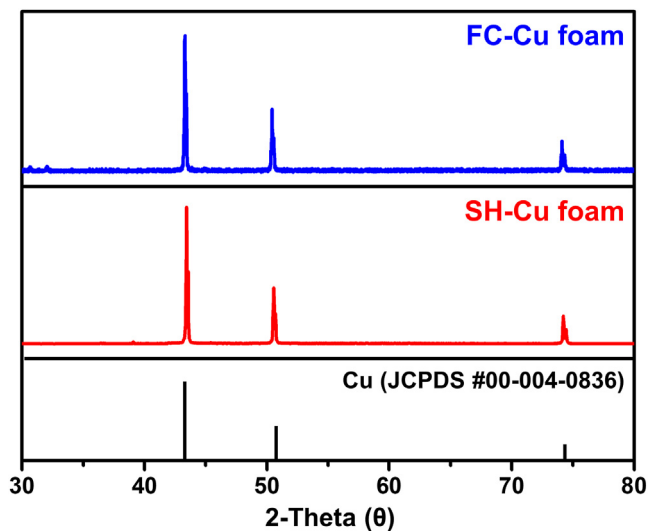


Fig. 2 – XRD patterns of Cu foams processed by FC (blue colored) and SH (red colored) methods. The peaks were identified according to the card JCPDS 00-004-0836.

respectively. The Cu walls (16 ± 7 μ m in thickness) and near-polygonal pores (84 ± 26 μ m in diameter) were interconnected in the entire SH-Cu foam without other impurities after selective removal of the spacer (NaCl) into warm water (~90 °C). It should be emphasized that the structure of the pores and struts in the SH-Cu foam is relatively isotropic, compared to the FC-Cu foam, even if the pores and struts observed on the longitudinal surface are slightly tilted along the vertical loading direction. Single struts of the SH-Cu foam are shown in the insets of Fig. 3b and d. It can be seen that the struts are composed of several sintered powder particles in the form of bead-connected ligaments. The calculated overall porosities of the FC- and SH-Cu foams were 63–73 and 70–77%, respectively. Figure 3e and 3f shows the microstructures of the polished and etched struts of the FC- and SH-Cu foams. After being etched with Livingston's etchant (30 ml HCl, 10 ml acetic acid, and 410 ml deionized water) [32], individual grains are observed on the struts of both Cu foams. The average grain size of FC- and SH-Cu foams was measured by Image-Pro software, resulting in 1.6 ± 0.9 and 12 ± 6 μ m, respectively. This is most likely because the final grain size of FC- and SH-Cu foams is affected by the particle size of the starting powder (~40 nm vs. ~11 μ m). As a result, a significant difference in the pore and grain size of FC- and SH-Cu foams can affect the mechanical properties.

Compressive stress–strain curves are shown in Fig. 4 for the FC- and SH-Cu foams with the loading axis being parallel to the freezing direction and the cold-pressing direction, respectively. The values of the compressive yield strength determined as 0.2% offset flow stress are listed in Table 1. Both Cu foams exhibit a typical compressive behavior of metallic foams: an initial linear elastic stage, a plastic plateau regime, and a densification region with steeply rising stresses as the compression progresses [37]. In particular, the repeated stress–strain behavior shows excellent reproducibility, despite a small difference in porosity between the Cu foams manufactured by the same process.

It is clearly seen from Fig. 4 that the SH-Cu foam showed a rather smooth compressive mechanical behavior; by contrast, a non-monotonous stress variation was observed for the FC-Cu foam despite similar porosity. This is because different deformation modes take place within the FC- and SH-Cu foams during compression. The FC-Cu foam exhibited a stress drop at the strain of about 3%, and then the stress increased again with increasing strain. It is hypothesized that the stress drop for the FC-foam was caused by the plastic buckling of the longitudinally loaded struts owing to its anisotropic elongated pore structure (i.e., parallel to the loading direction) [20,22]. On the other hand, in the case of the SH-Cu foam, the stress was gradually changed from the elastic region to the plastic region. An initial homogeneous deformation occurred in the entire specimen, followed by collapsing and compaction, thus resulting in the smooth plateau region in good agreement with previous reports [38–41]. Despite their similar porosities, the compressive yield strength and the flow stress were much higher for the FC-Cu foam than for the SH-Cu foam. Here, we can consider several possible explanations for the much greater strength of the FC-Cu foam than that of the SH-Cu foam. First, the pore size and grain size of the struts have a considerable effect on

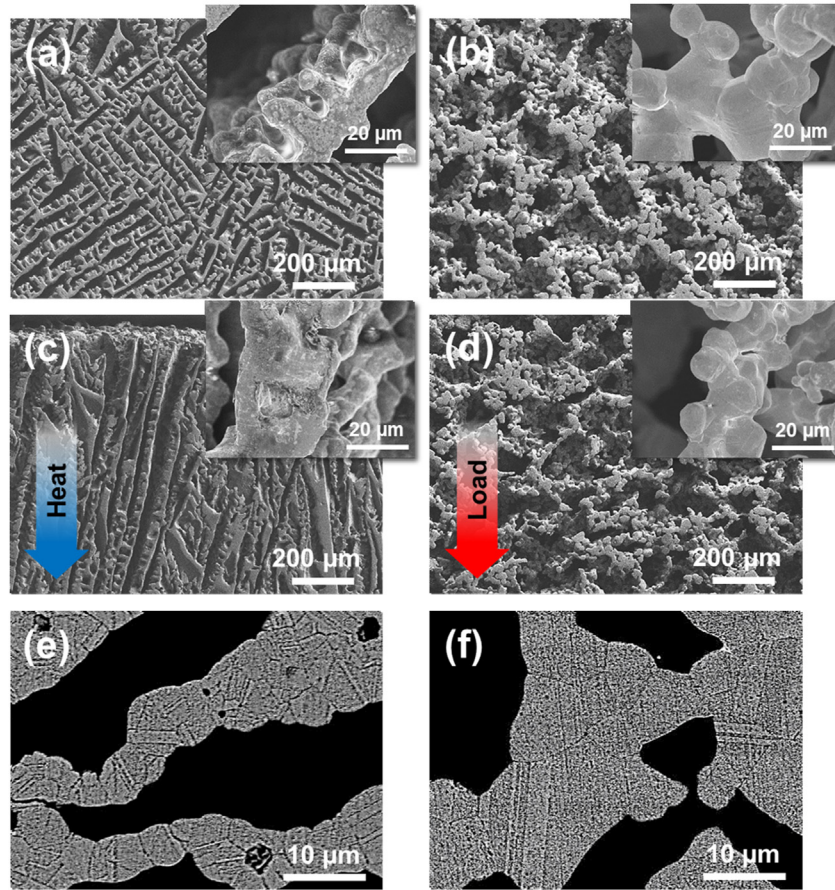


Fig. 3 – SEM images for (a, b) radial section and (c, d) longitudinal section of (a, c) FC- and (b, d) SH-Cu foams. The heat flow and the compressive loading directions for FC- and SH-Cu foams are indicated by blue and red arrows in (c) and (d), respectively. Magnified images are also shown in the insets of (a–d). Optical images of polished and chemically etched surface of (e) FC- and (f) SH-Cu foams: the surface was treated by Livingston’s etchant [23] to reveal the grains in the struts of the Cu foams.

the compressive strength. The significant difference in the pore size (FC: $13 \pm 8 \mu\text{m}$, SH: $84 \pm 26 \mu\text{m}$) might have contributed to the difference in the mechanical strength of the FC- and SH-Cu foams [42,43]. In terms of the grain size (Table 1), the struts of the FC-Cu foam (Fig. 3e) were comprised of grains that were much smaller (1.6 ± 0.9 vs. $12 \pm 6 \mu\text{m}$) than those of the SH-Cu foam (Fig. 3f); here, the difference in the strut widths (12 ± 5 vs. $16 \pm 7 \mu\text{m}$) was almost negligible compared

to the difference in the grain size. Another difference is that the struts of the FC-Cu foam were constructed by hydrogen reduction and sintering of the nano-sized Cu oxide powder particles, whereas the struts of the SH-Cu foam were constructed by only sintering of micron-sized Cu powder particles under Ar flow. The differences in the size of the initial powder particles and the method of heat treatment used for the foam processing should have resulted in the different grain sizes of

Table 1 – List of Cu foam specimens for compression test showing their microstructural features (pore structure, porosity, pore size, strut width, and grain size) and compressive yield strength (0.2% offset stress).

Process	Specimen	Pore structure	Porosity (%)	Pore size (μm)	Strut width (μm)	Grain size (μm)	Yield strength (MPa)
Freeze-casting	1	Lamellar	71.8	13 ± 8	12 ± 5	1.6 ± 0.9	20.4
	2		72.8				20.0
	3		72.9				19.4
	4		63.1				29.4
	5		62.8				26.6
Space-holder	1	Polygonal	76.6	84 ± 26	16 ± 7	12 ± 6	1.5
	2		77.1				1.4
	3		72.9				2.3
	4		70.2				1.2

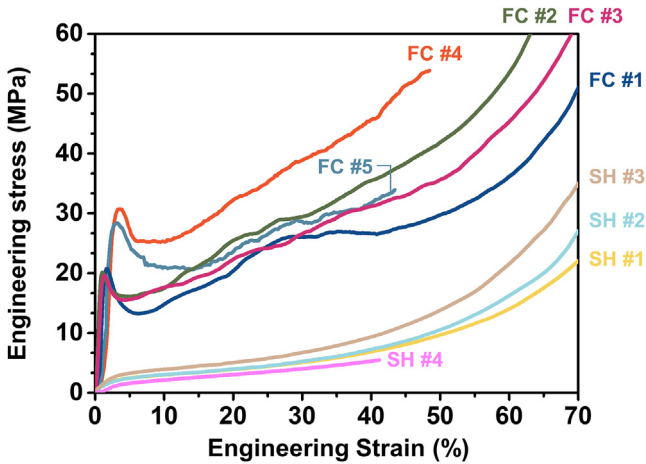


Fig. 4 – Comparison of compressive stress–strain curves obtained for FC- and SH-Cu foams (porosity: 63–73% and 70–77%) with the loading axis parallel to the freezing direction and the cold-pressing direction, respectively.

the Cu foams. It can be assumed that sintering between powders was more effective in the processing of FC-Cu foam owing to the presence of hydrogen gas than in the processing of SH-Cu foam under Ar gas.

Similar to bulk metals, the yield strength should be strongly influenced by the grain size of the struts; namely, it decreases with increasing grain size [44,45]. Therefore, the bulk yield strength of the struts in the SH-Cu foam may be much lower than that of the FC-Cu foam. It is possible to estimate the correct bulk yield strength from the grain size observed in Fig. 3e and f. From the Hall–Petch equation, we can estimate the yield strength of the struts (σ_{strut}) for the FC- and SH-Cu foams as:

$$\sigma_{strut} = \sigma_f + kd^{-1/2}, \quad (1)$$

where σ_f is the friction stress ($\sigma_f = 25$ MPa [46]), d is the average grain size in the struts and k is a constant (158 MPa $\mu\text{m}^{1/2}$ [37]). Using the grain sizes of 1.6 and 12 μm for FC- and SH-Cu foams, the strut yield strength of 150 and 71 MPa are estimated, respectively. This indicates that the two times higher theoretical yield strength of the directional struts of the FC-Cu foam (due to 7.5 times smaller mean grain size) may have also contributed significantly to its ~20 times higher compressive yield strength as compared to that of the SH-Cu foam [47,48].

Furthermore, it is reasonable to consider the effect of Cu oxide layer on the compressive yield strength, as Cu foams processed via both the FC and SH methods are assumed to possess more than an order of magnitude larger surface area than their bulk counterpart. The oxygen content in metals and alloys can play a dramatic role in some cases; for example, the strength of the bulk Cu can increase by up to 22% with increasing oxygen content; former studies have shown that the value of the yield strength of the bulk Cu can increase from 176 to 215 MPa when bulk Cu contains ~250 ppm solute oxygen [49–51]. As shown in Fig. 5, XPS analysis of the FC- and SH-Cu foams was carried out to characterize the surface states of the foams. In the FC- and SH-Cu foams before and after compression, the presence of Cu and O was clearly observable

from the XPS survey spectra (Fig. 5a), and the presence of Cu oxide on the surface of the FC- and SH-Cu foams could be verified from the Cu 2p spectra (Fig. 5b) both before and after compression; in particular, Cu 2p_{1/2} and Cu 2p_{3/2} peaks were located at the binding energy positions of around 952.3 and 932.5 eV, respectively, in both cases of FC- and SH-Cu foams. This result indicates that the native oxide with a major composition of Cu₂O was formed on the surfaces of the FC- and SH-Cu foams during the exposure to air [52]. Thus, the solute oxygen concentration is not significant, and therefore its contribution to the strength is marginal. It is highly unlikely that the large amounts of oxide layers formed on the surfaces of both the FC- and SH-Cu foams directly contributed to the compressive yield strength values of the Cu foam samples, although those excessive oxide layers due to the large surface area may have affected their compressive behaviors and fracture modes.

Additionally, the considerable difference in the pore morphology between the two types of Cu foams is closely linked to the significant difference between the yield strength values of the FC- and SH-Cu foams despite the similar porosity [53]. Here, the normalized yield strength of the Cu foams was predicted and compared by the Gibson–Ashby (G-A) model [54] and the cellular-lattice-structure (C-L) model [22] using the following formulas, respectively:

$$\frac{\sigma^*}{\sigma^0} = A_1 \left(\frac{\rho^*}{\rho^0} \right)^{1.5}, \quad (2)$$

$$\frac{\sigma^*}{\sigma^0} = A_2 \left(\frac{\rho^*}{\rho^0} \right), \quad (3)$$

where A_1 and A_2 are a constant generally being equal to 0.3 and 0.5 for porous metals, respectively. σ^0 and ρ^0 are the yield strength and density of the corresponding bulk material, and σ^* and ρ^* are the measured yield strength and density of the studied foams, respectively. The ρ^0 of Cu is taken as 8.96 g cm⁻³ while σ^0 depends on the grain size of the struts as discussed above [49]. Thus, σ^0 is taken as the yield strength of the struts (σ_{strut}) determined from eq. (1).

Besides G-A and C-L models, Tuncer et al. [55] reported an empirical prediction (labeled as Tuncer's formula), based on the type of different aspect ratios or morphology of the pores for SH-Ti foams. The corresponding formula was thus used for the calculation of normalized yield strength:

$$\frac{\sigma^*}{\sigma^0} = A_3 \left(\frac{\rho^*}{\rho^0} \right)^{2.28}, \quad (4)$$

where A_3 is a constant equal to 1.07, respectively. The values of the normalized yield strength (σ^*/σ^0) obtained for the FC- and SH-Cu foam specimens were plotted against the relative density (ρ^*/ρ^0) in Fig. 6 in a double-logarithmic manner, using the formulas given in eqs. (2)–(4).

In Fig. 6, the normalized yield strength values of FC-Cu foams being higher than those predicted by G-A and Tuncer's formulas are in close agreement with the C-L model: the G-A model was developed under the assumption of relatively weak-structured struts experiencing deformation with the bending, while the C-L model was constructed based on the stronger columnar struts with square cross section, experiencing deformation with the compression on the vertical

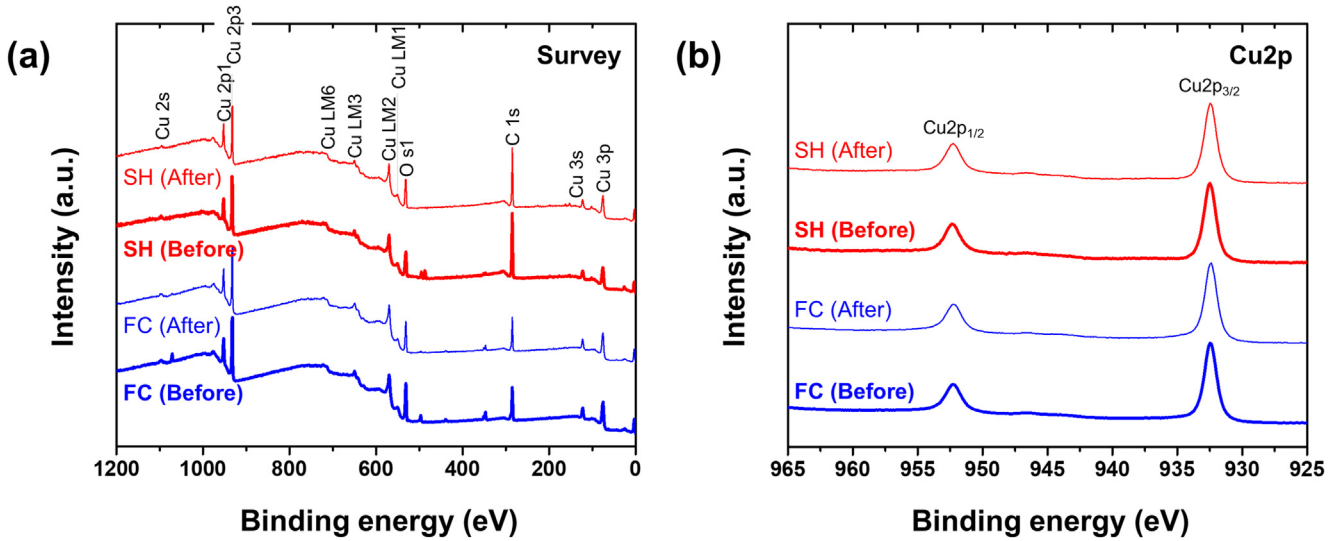


Fig. 5 – XPS pattern analysis of Cu foams processed by FC (blue colored) and SH (red colored) methods before and after compression testing; (a) survey spectra and (b) Cu2p core-level spectra. The thick and thin lines indicate the results before and after the compression testing, respectively.

struts. Based on the strut morphological similarity, the yield strength of the FC-Cu foams is apparently in better agreement with the C-L prediction than with the G-A model, whereas the normalized yield strength values of the SH-Cu foam are much lower than the predicted strength values with the primary deformation mechanism being bending and plastic yielding during compression [40]. Given that pore morphology of the SH-Cu foam is similar to that of the SH-Ti foam studied in [55], the Tuncer's empirical formula was expected to best predict the yield strength values of the SH-Cu foams; however, the SH-Cu foam data are still under the straight line representing the Tuncer's formula. Nevertheless, it can be seen that the normalized experimental yield strength values for the SH-Cu foam data plotted in Fig. 6 are along the slope of Tuncer's prediction for which the value of the exponent was taken as

2.28. The coefficient of the Tuncer's formula was modified from 1.07 to 0.6, resulting in best fitting line between the SH-Cu foam data and the modified Tuncer's prediction. This lower value of the coefficient can be attributed to the over-estimation of the strut yield strength using the Hall–Petch formula in eq. (1) since in some places the struts of the SH-Cu foam have a one-grain thickness, as shown at the left side of the bottom of Fig. 3f. Therefore, a considerable amount of boundaries of the grains is on the strut surfaces, and thus they have no such a strengthening effect as it is usual inside bulk materials. As a consequence, the strut material may be softer than the yield strength estimated from the grain size using the Hall–Petch formula, and the normalized strength is underestimated for all SH-Cu foams in our calculation, leading to a lower coefficient in the modified Tuncer's formula.

It is also worth comparing the energy absorbed during compression for the FC- and SH-Cu foams. This quantity can be determined by the integration of the stress–strain curve [56]:

$$W = \int_0^{\epsilon_D} \sigma(\epsilon) d\epsilon, \quad (5)$$

where W is the absorbed energy per unit volume and ϵ_D is the densification strain was selected as 50% in accordance with standard ISO 13314:2011. From the compressive stress–strain curves, the absorbed energy up to the strain of 50% was determined from eq. (5) and represented as vertical bars in Fig. 7. It can be seen that the absorbed energy for the FC-Cu foam is ~4.6 times higher than that of the SH-Cu foam (FC: 12.3 MJ m⁻³, SH: 2.7 MJ m⁻³), in line with the much higher compressive yield strength of FC-Cu foam (FC: 19–29 MPa, SH: 1.2–2.3 MPa).

To further analyze the compressive behavior of the Cu foams, in-situ video recording and AE measurements were conducted during compression. The representative compression curves with simultaneously recorded AE response up to

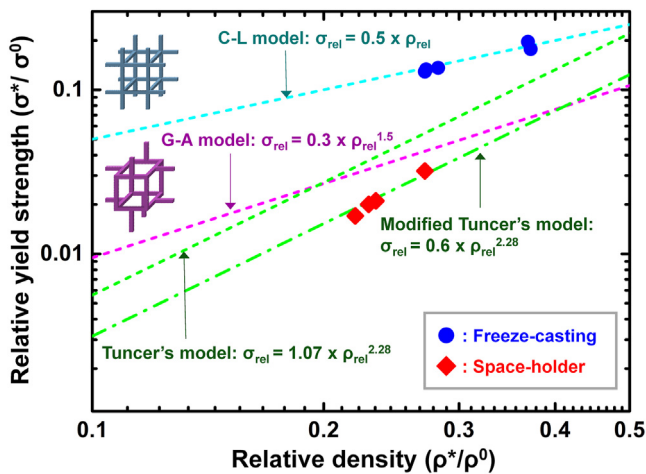


Fig. 6 – Plot of relative yield strength versus relative density to compare experimentally obtained data with model calculations.

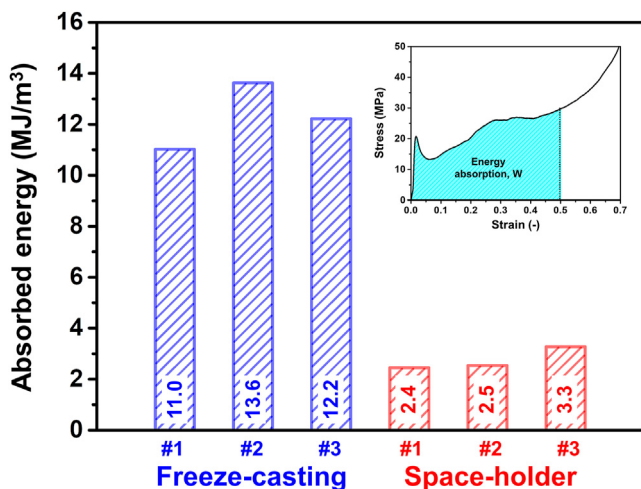


Fig. 7 – Absorbed energy and densification% during compression of FC- and SH-Cu foams. The absorbed energy values were determined by measuring the area under the stress–strain curves recorded from the beginning of compression until the strain of 50%.

the strain of about 0.4 and images of the sample surface are shown in Fig. 8. As already discussed, the FC-Cu foam (Fig. 8a) exhibited a considerable stress drop after the peak stress (shortly after the yield point, at the strain of ~3%). The occurrence of this stress drop at this rather low degree of global deformation coincides with the onset of the shear band's formation (see the snapshots in Fig. 8a). It can be also observed that further plasticity concentrates in the vicinity of this shear band up until the end of the test, and the deformation band broadens as the sample progressively crushes. As a consequence, the bottom part of the sample remains practically intact. The AE response reflects this crushing behavior; the AE response consists of large amplitude–large energy signals resulting in “steps” in the cumulative AE energy curve. The likely origin of these signals is cracking since due to the small grain size, AE signals caused by dislocation motion within the grains are not measurable [57]. The cumulative number of AE events as a function of strain is nearly linear while the slope of the cumulative energy curve starts to decrease beyond 25% strain. Such an energy evolution can be attributed to high-energy signals occurring during the plateau (strain between ~5% – ~17%). Aside from the lower number of very high-energy signals during the strain hardening stage, the failure mechanism (i.e., crushing within a well-defined deformation band) and its AE characteristics remain unchanged until the end of the test for FC-Cu.

A dissimilar behavior in terms of both deformation dynamics and AE response is evidenced for SH-Cu foam (Fig. 8b). The snapshots bear witness of a very uniform deformation without any discernible strain localization, resulting in a smooth deformation curve. In contrast to FC-Cu foams, the AE activity (by means of the number of AE events) is weaker during the initial stages of loading, and rises with increasing strain. This is best visible in the convex shape of the cumulative AE energy curve (in contrast to the concave one for FC-Cu in Fig. 8a) and the cumulative number of events. Generally,

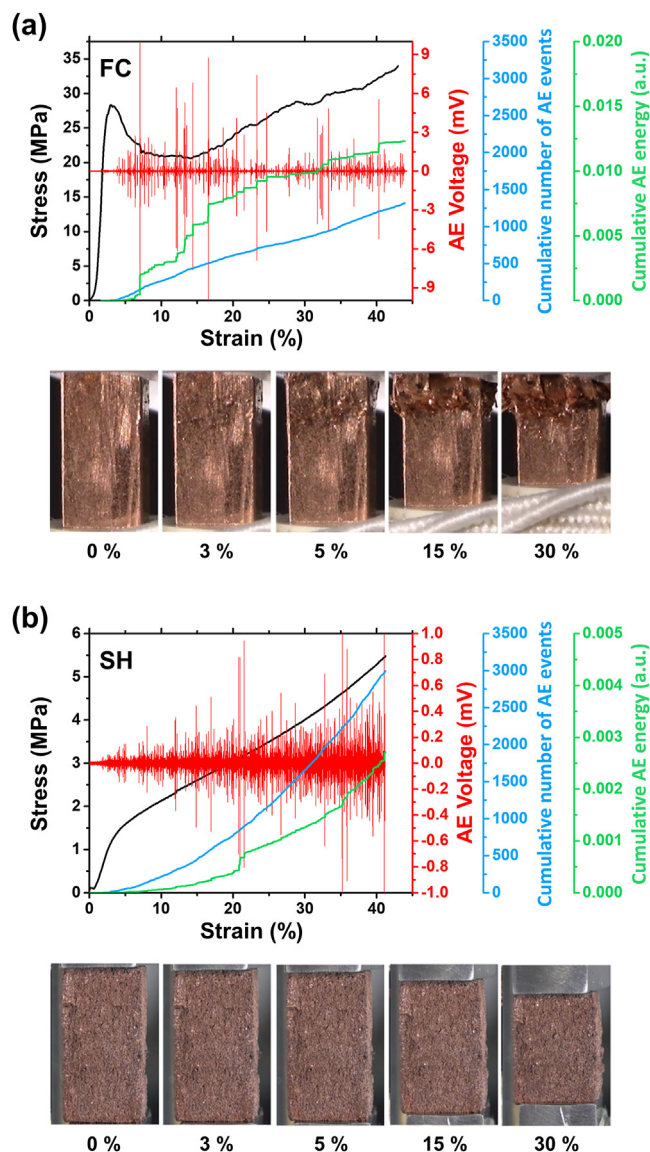


Fig. 8 – Compressive stress–strain curves (black line) and the AE response (the as-measured AE streaming (red), the number of events (blue) and the cumulative energy (green)) for (a) FC- and (b) SH-Cu foams. The snapshots show the deformation of the samples at strains of 0%, 3%, 5%, 15%, and 30%.

the AE response in the case of SH-Cu foams (i) is less intense (note differences in the scales in Fig. 8; the measured AE voltage is in the range of -1 mV– 1 mV for SH foam while it is -10 mV– 10 mV for FC foam) and (ii) consists of AE events mostly of lower energy, resulting in a relatively smooth cumulative AE energy curve. One of the reasons for measuring low energy signals is that in the case of SH foam the grain size is large enough the measure AE signals related to plastic deformation due to dislocation activity. These signals have lower amplitude than the signals due to fracture, especially at low strains, when the mean free path of moving dislocations is relatively high. The snapshots in Fig. 8b show that at higher

strain, fracture is visible on the surface, indicating that the increase in the number of higher energy AE signals are (at least partly) due to the collapse of the struts. The low fraction of higher amplitude signals suggests that the main failure mechanisms, especially at small strains, are related to collective dislocation motion. At higher strains, signals originated from fracture become more pronounced, suggesting changes in the failure mode.

These results thus support and complement the earlier discussion on the operating deformation mechanisms. The FC-Cu foams deform by a gradual well-localized (both in space and time) crushing of the struts (i.e., the local fracture events), giving rise to intermittent but relatively intense AE signals; on the other hand, the SH-Cu foams deform continuously and uniformly by means of lower energy plasticity modes – i.e., strut bending and buckling – related to correlated motion of dislocations, which is a common source of (macroscopically) continuously emitted AE signals [58].

4. Conclusions

Cu foams containing open-porous lamellar-structured and polygonal pores were successfully manufactured via FC and SH processes, respectively. Through the FC process, anisotropically stretched lamellar pores (~13 μm), and struts (~12 μm) were developed into Cu foam by a combination of sublimation of ice dendrite and hydrogen-reduction heat-treatment processes, and the struts consisted of ~1.6 μm sized Cu grains. Through the SH process, polygonal pore (~84 μm) and isotropically stretched random struts (~16 μm) were developed into Cu foam by a combination of heat treatment and selective removal of spacer (sodium chloride) processes and the struts consisted of ~12 μm sized Cu grains, being approximately 8 times greater than that of the struts in FC Cu foam.

Compression test of the parallelepiped Cu foams was performed at room temperature. Both Cu foams exhibited typical compressive deformation behavior of ductile porous metal, but several different compressive characteristic, such as the compressive yield strength (FC-Cu foam: 19–29 MPa, SH-Cu foam: 1.2–2.3 MPa) and the amount of absorbed energy during compression (FC-Cu foam: ~12.3 MJ m^{-3} , SH-Cu foam: ~2.7 MJ m^{-3}) were observed, which were originated from the morphological variations (e.g., pore size, grain size, and the directionality of pore and strut) caused by the difference in the starting powder type and the heat-treatment conditions.

The AE analysis and the video recordings of Cu foams showed different deformation mechanisms during compression in FC-Cu and SH-Cu foams. FC-Cu foam predominantly deformed by crushing within a single well-defined shear band, giving rise to intermittent but strong AE signals originating mostly from the fracture of the struts (especially during the plateau regime). By contrast, the deformation was much more homogeneous in the case of SH-Cu foams. The AE response was weaker and rather continuous due to the lower energy plasticity modes related to dislocation motion; thus, the main deformation mechanism was strut bending and/or buckling throughout the sample.

Data availability

The raw/processed data required to reproduce these findings cannot be shared at this time due to technical or time limitations.

Declaration of Competing Interest

The authors declare that they have no known competing financial interests or personal relationships that could have appeared to influence the work reported in this paper.

Acknowledgements

This research was supported by the Hungarian–Korean bilateral Research program (TÉT) No. 2018–2.1.17-TÉT-KR–2018–00003. This work was also supported by the ELTE Institutional Excellence Program (TKP2020-IKA-05) financed by the Hungarian Ministry of Human Capacities. This work was also supported by the János Bolyai Research Scholarship of the Hungarian Academy of Sciences and the ÚNKP-20-5 new national excellence program of the Ministry for Innovation and Technology from the source of the National Research, Development and Innovation Fund. HC and HP also acknowledge support from the Basic Science Research Program (NRF-2021R1A2C2006365; 2019R1I1A1A01058247) through the NRF of Korea. This work was also supported by the NRD Fund (TKP2020 IES, Grant No. BME-IE-NAT) based on the charter of bolster issued by the NRD Office under the auspices of the Ministry for Innovation and Technology.

REFERENCES

- [1] Davis JR. *ASM specialty handbook: copper and copper alloys*. Materials Park: ASM International; 2001.
- [2] Lahiri I, Oh S, Hwang J, Cho S, Sun Y, Banerjee R, et al. High capacity and excellent stability of lithium-ion battery anode using interface-controlled binder-free multiwall carbon nanotubes grown on copper. *ACS Nano* 2010;4:3440–6. <https://doi.org/10.1021/nn100400r>.
- [3] Lindstrom B, Pettersson LJ. Hydrogen generation by steam reforming of methanol over copper-based catalysts for fuel cell applications. *Int J Hydrogen Energy* 2001;26:923–33. [https://doi.org/10.1016/S0360-3199\(01\)00034-9](https://doi.org/10.1016/S0360-3199(01)00034-9).
- [4] Klapars A, Huang X, Buchwald SL. A general and efficient copper catalyst for the amidation of aryl halides. *J Am Chem Soc* 2002;124:7421–8. <https://doi.org/10.1021/ja0260465>.
- [5] Hui P, Tan H. Temperature distributions in a heat dissipation system using a cylindrical diamond heat spreader on a copper heat sink. *J Appl Phys* 1994;75:748–57. <https://doi.org/10.1063/1.356480>.
- [6] Ruparelia JP, Chatterjee AK, Duttagupta SP, Mukherji S. Strain specificity in antimicrobial activity of silver and copper nanoparticles. *Acta Biomater* 2008;4:707–16. <https://doi.org/10.1016/j.actbio.2007.11.006>.
- [7] Park H, Um JH, Choi H, Yoon W, Sung Y, Choe H. Hierarchical micro-lamella-structured 3D porous copper current collector coated with tin for advanced lithium-ion batteries. *Appl Surf Sci* 2017;399:132–8. <https://doi.org/10.1016/j.apsusc.2016.12.043>.

- [8] Li YH, Chang S, Liu XL, Huang JC, Yin JL, Wang GL, et al. Nanostructured CuO directly grown on copper foam and their supercapacitance performance. *Electrochim Acta* 2012;85:393–8. <https://doi.org/10.1016/j.electacta.2012.07.127>.
- [9] Chladek P, Croiset E, Epling W, Hudgins RR. Characterization of copper foam as catalytic material in ethanol dehydrogenation. *Can J Chem Eng* 2007;85:917–24. <https://doi.org/10.1002/cjce.5450850613>.
- [10] Chiba H, Ogushi T, Nakajima H, Ikeda T. Heat transfer capacity of lotus-type porous copper heat sink. *JSM Int J Ser B* 2004;47:516–21. <https://doi.org/10.1299/jsmeb.47.516>.
- [11] Zhao JH, Yan PH, Snow B, Santos RM, Chiang YW. Micro-structured copper and nickel metal foams for wastewater disinfection: proof-of-concept and scale-up. *Process Saf Environ Protect* 2020;142:191–202. <https://doi.org/10.1016/j.psep.2020.06.013>.
- [12] Hu H, Lai Z, Zhao Y. Heat transfer and pressure drop of refrigerant flow boiling in metal foam filled tubes with different wettability. *Int J Heat Mass Tran* 2021;177:121542. <https://doi.org/10.1016/j.ijheatmasstransfer.2021.121542>.
- [13] Hu H, Zhao Y, Lai Z, Hu C. Influence of surface wettability on pool boiling heat transfer on metal foam covers. *Int J Therm Sci* 2021;168:107069. <https://doi.org/10.1016/j.ijthermalsci.2021.107069>.
- [14] Hu H, Zhao Y, Lai Z, Hu C. Experimental investigation on nucleate pool boiling heat transfer characteristics on hydrophobic metal foam covers. *Appl Therm Eng* 2020;179:115730. <https://doi.org/10.1016/j.applthermaleng.2020.115730>.
- [15] Hu H, Lai Z, Ding G. Heat transfer and pressure drop characteristics of wet air flow in metal foam with hydrophobic coating under dehumidifying conditions. *Appl Therm Eng* 2018;132:651–64. <https://doi.org/10.1016/j.applthermaleng.2018.01.010>.
- [16] Hu H, Lai Z, Ding G, Zhuang D, Weng X. Experimental investigation on water drainage characteristics of open-cell metal foams with different wettabilities. *Int J Refrig* 2017;79:101–13. <https://doi.org/10.1016/j.ijrefrig.2017.04.002>.
- [17] Hu H, Weng X, Zhuang D, Ding G, Lai Z, Xu X. Heat transfer and pressure drop characteristics of wet air flow in metal foam under dehumidifying conditions. *Appl Therm Eng* 2016;93:1124–34. <https://doi.org/10.1016/j.applthermaleng.2015.09.019>.
- [18] Shin HC, Liu M. Copper foam structures with highly porous nanostructured walls. *Chem Mater* 2004;16:5460–4. <https://doi.org/10.1021/cm048887b>.
- [19] Kim JH, Kim RH, Kwon HS. Preparation of copper foam with 3-dimensionally interconnected spherical pore network by electrodeposition. *Electrochem Commun* 2008;10:1148–51. <https://doi.org/10.1016/j.elecom.2008.05.035>.
- [20] Hyun SK, Nakajima H. Anisotropic compressive properties of porous copper produced by unidirectional solidification. *Mater Sci Eng, A* 2003;340:258–64. [https://doi.org/10.1016/S0921-5093\(02\)00181-8](https://doi.org/10.1016/S0921-5093(02)00181-8).
- [21] Simone AE, Gibson LJ. The tensile strength of porous copper made by the GASAR process. *Acta Mater* 1996;44:1437–47. [https://doi.org/10.1016/1359-6454\(95\)00278-2](https://doi.org/10.1016/1359-6454(95)00278-2).
- [22] Park H, Choi M, Choe H, Dunand DC. Microstructure and compressive behavior of ice-templated copper foams with directional, lamellar pores. *Mater Sci Eng, A* 2017;679:435–45. <https://doi.org/10.1016/j.msea.2016.10.057>.
- [23] Jo H, Cho YH, Choi M, Cho J, Um JH, Sung YE, et al. Novel method of powder-based processing of copper nanofoams for their potential use in energy applications. *Mater Chem Phys* 2014;145:6–11. <https://doi.org/10.1016/j.matchemphys.2014.02.009>.
- [24] Parvanian A, Saadatfar M, Panjepour M, Kingston A, Sheppard A. The effects of manufacturing parameters on geometrical and mechanical properties of copper foams produced by space holder technique. *Mater Des* 2014;53:681–90. <https://doi.org/10.1016/j.matdes.2013.07.047>.
- [25] Ke X, Cheng Y, Liu J, Liu L, Wang N, Liu J, et al. Hierarchically bicontinuous porous copper as advanced 3d skeleton for stable lithium storage. *ACS Appl Mater Interfaces* 2018;10:13552–61. <https://doi.org/10.1021/acsami.8b01978>.
- [26] El-Hadek MA, Kaytbay S. Mechanical and physical characterization of copper foam. *Int J Mech Mater Des* 2008;4:63–9. <https://doi.org/10.1007/s10999-008-9058-2>.
- [27] Singh G, Pandey P. Uniform and graded copper open cell ordered foams fabricated by rapid manufacturing: surface morphology, mechanical properties and energy absorption capacity. *Mater Sci Eng, A* 2019;761:138035. <https://doi.org/10.1016/j.msea.2019.138035>.
- [28] Feng MN, Xie Y, Zhao CF, Luo Z. Microstructure and mechanical performance of ultrasonic spot welded open-cell Cu foam/Al joint. *J Manuf Process* 2018;33:86–95. <https://doi.org/10.1016/j.jmapro.2018.04.022>.
- [29] Yue XY, Wang WW, Wang QC, Meng JK, Wang XX, Song Y, et al. Cuprite-coated Cu foam skeleton host enabling lateral growth of lithium dendrites for advanced Li metal batteries. *Energy Storage Mater* 2019;21:180–9. <https://doi.org/10.1016/j.ensm.2018.12.007>.
- [30] Seki H, Tane M, Otsuka M, Nakajima H. Effects of pore morphology on fatigue strength and fracture surface of lotus-type porous copper. *J Mater Res* 2007;22:1331–8. <https://doi.org/10.1557/jmr.2007.0164>.
- [31] Chen J, Li XF, Li W, He JJ, Li C, Dai SW, et al. Study on the compression properties and deformation failure mechanism of open-cell copper foam. *Adv Eng Mater* 2017;19:1600861. <https://doi.org/10.1002/adem.201600861>.
- [32] Janeczek M, Hadzima B, Hellmig R, Estrin Y. The influence of microstructure on the corrosion properties of Cu polycrystals prepared by ECAP. *Kovove Mater* 2005;43:258–71.
- [33] Petrenko VF, Whitworth RW. *Physics of ice*. Oxford: Oxford University; 2002.
- [34] Jo H, Kim M, Choi H, Sung Y, Choe H, Dunand DC. Morphological study of directionally freeze-cast nickel foams. *Metall Mater Trans* 2016;3:46–54. <https://doi.org/10.1007/s40553-016-0068-y>.
- [35] Um JH, Choi M, Park H, Cho YH, Dunand DC, Choe H, et al. 3D macroporous electrode and high-performance in lithium-ion batteries using SnO₂ coated on Cu foam. *Sci Rep* 2016;6:18626. <https://doi.org/10.1038/srep18626>.
- [36] Park H, Noh Y, Choi H, Hong K, Kwon K, Choe H. Processing, microstructure, and oxidation behavior of iron foams. *Metall Mater Trans* 2016;47A:4760–6. <https://doi.org/10.1007/s11661-016-3601-9>.
- [37] Park H, Um T, Hong K, Kang JS, Nam HS, Kwon K, et al. Effects of powder carrier on the morphology and compressive strength of iron foams: water vs camphene. *Metall Mater Trans B* 2018;49:2182–90. <https://doi.org/10.1007/s11663-018-1302-z>.
- [38] Gibson LJ, Ashby MF. The mechanics of three-dimensional cellular materials. *Proc R Soc London, Ser A* 1982;382:43–59. <https://doi.org/10.1098/rspa.1982.0088>.
- [39] Brandes EA, Brook GB. *Smithells metals reference book*. 7th ed. Oxford: Butterworth-Heinemann; 1992.
- [40] Mondal DP, Jain H, Das S, Jha AK. Stainless steel foams made through powder metallurgy route using NH₄HCO₃ as space holder. *Mater Des* 2015;88:430–7. <https://doi.org/10.1016/j.matdes.2015.09.020>.
- [41] Jain H, Mondal DP, Gupta G, Kumar R. Effect of compressive strain rate on the deformation behaviour of austenitic stainless steel foam produced by space holder technique. *Mater Chem Phys* 2021;259:124010. <https://doi.org/10.1016/j.matchemphys.2020.124010>.

- [42] San Marchi C, Despois JF, Mortensen A. Uniaxial deformation of open-cell aluminum foam: the role of internal damage. *Acta Mater* 2004;52:2895–902. <https://doi.org/10.1016/j.actamat.2004.02.035>.
- [43] San Marchi C, Mortensen A. Deformation of open-cell aluminum foam. *Acta Mater* 2001;49:3959–69. [https://doi.org/10.1016/S1359-6454\(01\)00294-4](https://doi.org/10.1016/S1359-6454(01)00294-4).
- [44] Jiang B, Wang ZJ, Zhao NQ. Effect of pore size and relative density on the mechanical properties of open cell aluminum foams. *Scripta Mater* 2007;56:169–72. <https://doi.org/10.1016/j.scriptamat.2006.08.070>.
- [45] Wen CE, Yamada Y, Shimojuma K, Chino Y, Hosokawa H, Mabuchi M. Compressibility of porous magnesium foam: dependency on porosity and pore size. *Mater Lett* 2004;58:357–60. [https://doi.org/10.1016/S0167-577X\(03\)00500-7](https://doi.org/10.1016/S0167-577X(03)00500-7).
- [46] Goussery V, Bienvenu Forest S, Gourgues AF, Colin C, Bartout JD. Grain size effects on the mechanical behavior of open-cell nickel foams. *Adv Eng Mater* 2004;6(6):432–9. <https://doi.org/10.1002/adem.200405153>.
- [47] Gubicza J, Jenei P, Nam K, Kádár C, Jo H, Choe H. Compressive behavior of Cu-Ni alloy foams: effects of grain size, porosity, pore directionality and chemical composition. *Mater Sci Eng, A* 2018;725:160–70. <https://doi.org/10.1016/j.msea.2018.04.018>.
- [48] Gubicza J. *Defect structure and properties of nanomaterials*. 2nd ed. Swaston: Woodhead Publishing; 2017.
- [49] Zhang EL, Wang B. On the compressive behaviour of sintered porous coppers with low to medium porosities - Part I: experimental study. *Int J Mech Sci* 2005;47:744–56. <https://doi.org/10.1016/j.ijmecsci.2004.12.011>.
- [50] Wang YC, Huang H, Jia GZ, Ke GZ, Zhang J, Yuan GY. Effect of grain size on the mechanical properties of Mg foams. *J Mater Sci Technol* 2020;58:46–54. <https://doi.org/10.1016/j.jmst.2020.03.067>.
- [51] Gusković D, Marković D, Nestorović S. Effect of deformation and oxygen content on mechanical properties of different copper wires. *Bull Mater Sci* 1997;20:693–7. <https://doi.org/10.1007/BF02745077>.
- [52] Kapoor G, Kvackaj T, Heczal A, Bidulska J, Kocisko R, Fogarassy Z, et al. The influence of severe plastic deformation and subsequent annealing on the microstructure and hardness of a Cu-Cr-Zr alloy. *Materials* 2020;13:2241. <https://doi.org/10.3390/ma13102241>.
- [53] Kuang M, Li TT, Chen H, Zhang SM, Zhang LL, Zhang YX. Hierarchical Cu₂O/CuO/Co₃O₄ core-shell nanowires: synthesis and electrochemical properties. *Nanotechnology* 2015;26:304002. <https://doi.org/10.1088/0957-4484/26/30/304002>.
- [54] Hakamata M, Asao Y, Kuromura T, Chen YQ, Kusuda H, Mabuchi M. Density dependence of the compressive properties of porous copper over a wide density range. *Acta Mater* 2007;55:2291–9. <https://doi.org/10.1016/j.actamat.2006.11.024>.
- [55] Tuncer N, Arslan G, Maire E, Salvo L. Influence of cell aspect ratio on architecture and compressive strength of titanium foams. *Mater Sci Eng, A* 2001;528:7368–74. <https://doi.org/10.1016/j.msea.2011.06.028>.
- [56] Gibson LJ, Ashby MF. *Cellular solids: structures and properties*. Cambridge: Cambridge University; 1997.
- [57] Heiple CR, Carpenter SH. Acoustic emission produced by deformation of metals and alloys - a review. *J Acoust Emiss* 1987;6:177–204.
- [58] Máthis K, Chmelík F. Exploring plastic deformation of metallic materials by the acoustic emission technique. In: *Acoustic emission*. Rijeka: Intech; 2012.